Research Square

Preprints are preliminary reports that have not undergone peer review.
They should not be considered conclusive, used to inform clinical practice,
or referenced by the media as validated information.

AI-Driven Detection and Classification of Micro-Deformations on Industrial Freeform Surfaces Using Handheld Laser Scanning, Signed Distance Fields, and Point Cloud Deep Learning

Shah Wali Nazari

eng10501@gmail.com

Zonguldak Bülent Ecevit University

Veli Akarsu

Zonguldak Bülent Ecevit University

Hakan Akçın

Zonguldak Bülent Ecevit University

Murat Yakar

Mersin University

Research Article

Keywords: Handheld laser scanning, Signed Distance Field, PointNet, Micro-deformation detection, Industrial quality control, Point cloud deep learning

Posted Date: June 23rd, 2026

DOI: https://doi.org/10.21203/rs.3.rs-9782848/v1

License: This work is licensed under a Creative Commons Attribution 4.0 International License.
Read Full License

Additional Declarations: No competing interests reported.

AI-Driven Detection and Classification of Micro-Deformations on Industrial Freeform Surfaces Using Handheld Laser Scanning, Signed Distance Fields, and Point Cloud Deep Learning

Shah Wali Nazari · Veli Akarsu · Hakan Akçın · Murat Yakar

Shah Wali Nazari (corresponding author) · eng10501@gmail.com

[1] Department of Geomatics Engineering, Graduate School of Natural and Applied Sciences, Zonguldak Bulent Ecevit University, Zonguldak, Türkiye

[2] Department of Architecture and Urban Planning, Zonguldak Vocational School, Zonguldak Bulent Ecevit University, Zonguldak, Türkiye

[3] Department of Geomatics Engineering, Graduate School of Natural and Applied Sciences, Zonguldak Bulent Ecevit University, Zonguldak, Türkiye

[4] Department of Geomatics Engineering, Faculty of Engineering, Mersin University, Mersin, Türkiye

Received: date / Accepted: date / Published online: date

© The Author(s) year

Abstract

Industrial quality control is shifting from manual inspection toward automated workflows that combine handheld laser scanning (HLS) with deep learning. We present an end-to-end pipeline for detecting and classifying micro-deformations on industrial freeform surfaces. A Creaform HandySCAN Black Series triangulation scanner (volumetric accuracy 0.020 mm + 0.040 mm/m) acquired dense point clouds of two parts: a precision-machined metallic rotor and a carbon fiber-reinforced (CFRP) aviation panel. Signed distance fields (SDF) were computed by projecting each scan point onto its closest CAD surface patch. To rule out software-specific bias, the same SDF analysis was repeated in four metrology platforms (CloudCompare with M3C2, Geomagic Control X, PolyWorks Inspector, and MeshLab); all four agreed within 0.115–0.179 mm RMS. Deformation candidates were extracted with DBSCAN ($\varepsilon = 0.4$ mm, min_samples = 20) and region-growing segmentation, yielding 858 clusters. Each cluster was passed to a PointNet classifier with a seven-dimensional input combining XYZ coordinates, surface normals, and SDF values. Three classical baselines (SVM, Random Forest, MLP) were trained on hand-crafted features for comparison. PointNet reached 96.8% accuracy, a macro F1 of 0.95, and a false-negative rate of 2.1%, beating the best classical model (Random Forest, 94.1%) by 2.7 percentage points. The pipeline reliably detects defects below the 0.05 mm tolerance threshold and offers a practical Quality 4.0 inspection workflow for aerospace and defense manufacturing.

Keywords Handheld laser scanning · Signed Distance Field · PointNet · Micro-deformation detection · Industrial quality control · Point cloud deep learning

1 Introduction

1.1 Background and Motivation

Quality control in modern manufacturing is changing fast. Industry 4.0 calls for production lines that not only build parts but also inspect them automatically, feeding the results back into design and process control loops in near-real time (Javaid et al. 2022; Du et al. 2025). The bar is highest in aerospace, defense, and precision machining, where tolerances often sit below 0.1 mm across complex freeform surfaces (Chen et al. 2024).

Conventional metrology struggles at this scale. Visual inspection is operator-dependent and slow. Coordinate measuring machines (CMMs) are accurate but contact-based, point-by-point, and poorly suited to large or assembled components. Photogrammetry covers more surface but depends heavily on lighting and texture. None of these methods plug naturally into the closed-loop data infrastructure that Industry 4.0 assumes.

Triangulation-based handheld laser scanning (HLS) has emerged as the practical alternative for sub-millimeter inspection. Modern HLS systems reach volumetric accuracies below 0.025 mm (Cakmak et al. 2022; Suchocki et al. 2025) and capture full surface coverage in minutes rather than hours. Because the scanner moves rather than the part, operators can measure assembled or oversized components in situ. Guo et al. (2025) and Tan et al. (2025) showed that point clouds from such scanners feed directly into digital twin workflows, where as-built geometry is compared against as-designed CAD models to flag manufacturing drift. An early Turkish example by Bayram and Poyraz (2009) demonstrated that optical laser scanning can recover

the geometry of a damaged automotive part, anticipating the present industrial use case.

What remains underdeveloped is the next step: turning a deviation map into an automated pass/fail decision. In most current workflows, an inspector examines the color-coded map and judges whether the part is acceptable. That step is slow, subjective, and hard to scale. Deep learning models that operate directly on point clouds (Guo et al. 2020; Du et al. 2025) close this gap by learning the visual signature of defects from labeled examples. This paper combines HLS scanning, SDF-based deviation analysis, density-based clustering, and a PointNet classifier into one inspection pipeline, and benchmarks it on two industrial parts.

1.2 Literature Review

1.2.1 Handheld Laser Scanning in Industrial Surface Metrology

Bonin et al. (2021) benchmarked a handheld scanner against a pseudo-3D ball-lattice artifact and found accuracy varies sharply with reference geometry and stand-off distance. Setiawan et al. (2023) reported notable error growth in portable scanners when measuring holes below 5 mm diameter in metal specimens. Li et al. (2019) achieved near-micrometer accuracy after PCL-based noise reduction. Adams et al. (2024) compared scanning technologies across materials and concluded that surface reflectivity and acquisition parameters dominate the error budget.

Suchocki et al. (2025) coupled handheld 3D scanning with high-resolution digital microscopy and confirmed reliable detection of deformations above 0.05 mm, the threshold we adopt here. Cakmak et al. (2022) measured field accuracies of 0.08–0.15 mm in standard industrial environments. Idrobo-Pizo et al. (2019) gave the calibration framework for triangulation scanners mounted on robotic arms, and Soudarissanane et al. (2020) quantified how scan geometry, stand-off, and incidence angle govern point cloud quality.

In Turkish geomatics, Yakar et al. (2016), Karabacak and Yakar (2023), and Gur and Yakar (2024) established procedures for laser scanning of complex structures from heritage to forensic scenes. Their protocols, including scan planning, controlled pass overlap, and outlier filtering, were carried over into the industrial acquisition workflow in this paper (Ulvi et al. 2020; Yigit et al. 2021; Akcin et al. 2010).

1.2.2 Point Cloud Deep Learning for Industrial Defect Detection

Guo et al. (2020) reviewed deep learning on 3D point clouds and identified PointNet, PointNet++, DGCNN, and transformer-based variants as the leading architectures. PointNet (Qi et al. 2017) operates on raw, unordered point sets and remains a strong baseline because of its permutation invariance and tolerance for variable input size.

Recent applications confirm the maturity of the field. Jing and Wang (2023) used a transformer-based local embedding to segment defects in industrial point clouds. Garcia et al. (2024) trained fully convolutional networks for defect detection on complex metal surfaces. Arcano-Bea et al. (2026) benchmarked VAE, FoldingNet, DGCNN, and PointNet++ for reconstruction-based anomaly detection in shipbuilding sub-assemblies. Liu et al. (2024) presented a lightweight, model-free anomaly detector for production environments, and Xu (2025) fused RGB images with 3D features to keep performance stable when one sensor degrades. Du et al. (2025) provide a recent survey of 3D vision-based anomaly detection across manufacturing tasks. For aerospace composites, Catalucci et al. (2018) showed that automated inspection methods can capture manufacturing defects in composite aircraft components, which directly motivates our extension to a CFRP panel.

1.2.3 Signed Distance Fields and Deviation Algorithms

Signed distance fields measure the perpendicular distance from each scan point to a reference surface, carrying a sign to distinguish bulges from depressions. Cuesta et al. (2022) showed that point-cloud-to-CAD alignment quality determines deviation map fidelity. Giganto et al. (2020) reported that material reflectivity and surface roughness drive deviation noise in selective laser melting parts. Gundeti (2026) used a similar pipeline for reverse engineering automotive casting geometries.

Lague et al. (2013) introduced the M3C2 algorithm, which computes deviations along locally estimated surface normals and supplies a confidence interval based on point cloud roughness. M3C2 is now standard in geomonitoring and has migrated steadily into industrial inspection (Tan et al. 2025). Yang and Schwieger (2023) extended it with a patch-based variant that lowers uncertainty in complex topographies. For software comparison, Gapinski et al. (2014) established a benchmark protocol between PolyWorks and MeshLab that informs our cross-software section. Hegedus-Kuti et al. (2023) clustered M3C2 distances with DBSCAN to identify welding defects against ISO 5817:2014 classes, a workflow closely related to ours, although applied to weld seams rather than freeform surfaces. The contribution of the present work is to take SDF values one step further and feed them as input features into a PointNet classifier, rather than using them only as a deviation visualization.

1.3 Research Objectives and Contributions

We make four contributions:

- An end-to-end inspection pipeline that combines HLS acquisition, SDF computation, DBSCAN clustering, and PointNet classification for binary defect identification on industrial freeform surfaces.
- A systematic test of SDF values as an explicit feature channel for point cloud deep learning, alongside XYZ coordinates and surface normals.
- A side-by-side benchmark of classical machine learning (SVM, Random Forest, MLP) against PointNet on the same 858-cluster dataset.
- A cross-validation of the SDF pipeline across four metrology platforms (CloudCompare, Geomagic Control X, PolyWorks Inspector, MeshLab), showing agreement within 0.115–0.179 mm RMS on the same input.

2 Material and Methods

2.1 Sensor System

We used the Creaform HandySCAN Black Series. It projects 11 blue laser crosses onto the target surface and recovers depth from dual cameras through the standard triangulation relation (Idrobo-Pizo et al. 2019):

$$Z = (f_l \cdot B) / (p + f_l \cdot \cot(\theta)) \quad (1)$$

Z is the depth from the sensor to the surface, f_l is the camera focal length, B is the baseline between laser and camera, θ is the projection angle, and p is the position of the laser spot on the image sensor. The system operates between 100 and 400 mm stand-off and delivers a volumetric accuracy of 0.020 mm + 0.040 mm/m. We kept stand-off distance and incidence angle in narrow bands to minimize the geometry-driven error terms documented by Soudarissanane et al. (2020).

2.2 Test Components

We selected two parts with contrasting geometry and material behavior. The first is a precision-machined metallic rotor (735,253 vertices; 4,999,736 raw points; 400 × 400 × 30 mm bounding box), typical of rotating components in aerospace and automotive drivetrains. The second is a carbon fiber-reinforced polymer (CFRP) aviation panel (32,900,121 points; 1,217,859 vertices; 396 × 397 × 150 mm), representative of fuselage skins on UAVs and manned aircraft (Catalucci et al. 2018; Ulvi et al. 2020). The 65.7% jump in vertex count between the two parts gives a direct test of how the pipeline scales with geometric complexity. Figure 1 shows both components side by side in CloudCompare.

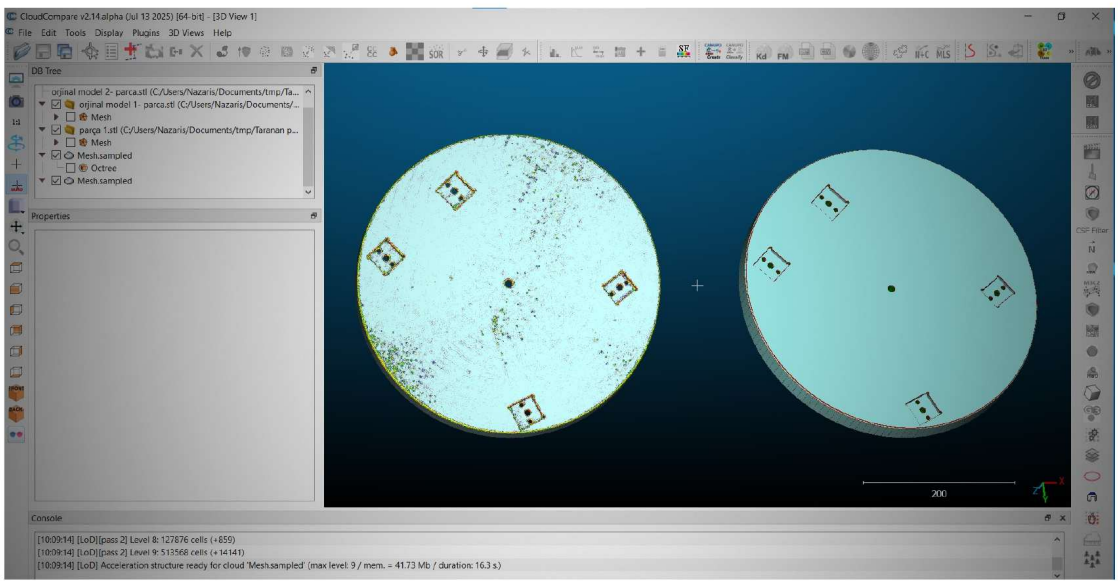


Fig. 1 Side-by-side comparison of the two experimental components in CloudCompare: as-built scanned point cloud of the metallic rotor (left, 16,450,662 pts, Roughness scalar field) alongside the as-designed CAD reference model (right)

2.3 Data Acquisition and Preprocessing

The scan protocol kept resolution and coverage uniform across both parts. Photogrammetric targets were placed on each component for automatic self-referencing. The operator made multiple overlapping passes at a 250 mm stand-off, perpendicular to the surface and below 200 mm/s. Raw point clouds were cleaned with statistical outlier removal (SOR) to suppress diffraction noise. Each as-built cloud was then aligned to its as-designed CAD model using the ICP algorithm (Besl and McKay 1992). Figure 2 shows the CloudCompare registration dialog: final RMS of 0.114866 mm over 50,000 correspondence points, with a 100% theoretical overlap and a near-identity transformation matrix.

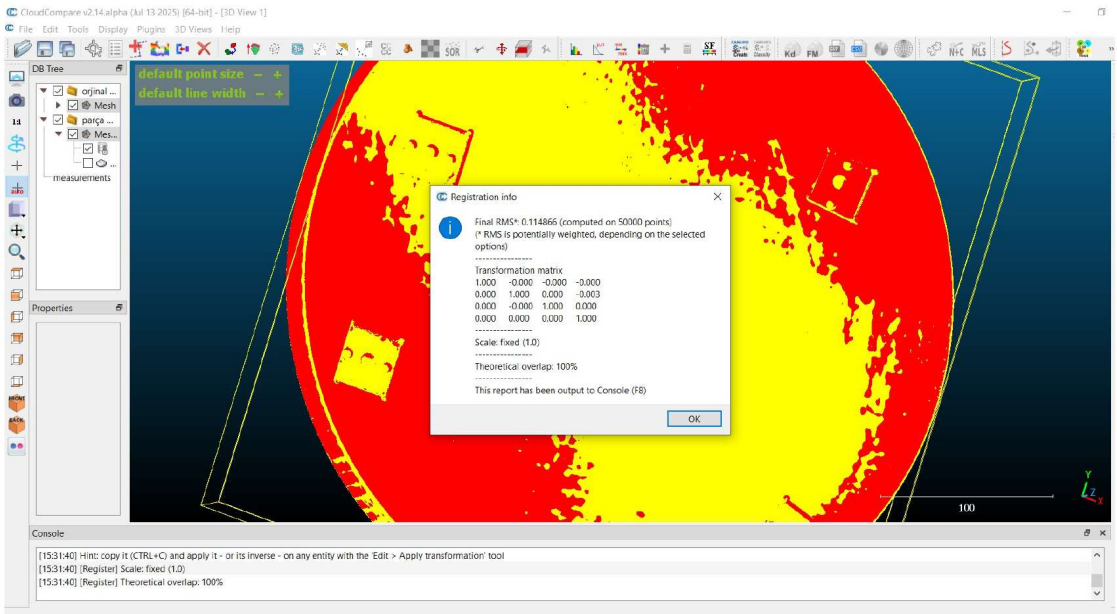


Fig. 2 CloudCompare ICP Registration info dialog; final RMS* = 0.114866 mm computed on 50,000 correspondence points; theoretical overlap 100%

2.4 Signed Distance Field Computation

After registration, each scan point p_i was projected onto the closest CAD surface patch to obtain its signed deviation:

$$d_i = \hat{n} \cdot (p_i - q_i) \quad (2)$$

Here q_i is the closest point on the CAD surface and $\hat{n}$ is the outward normal at q_i. A positive d_i indicates material excess; a negative one indicates loss. We used the M3C2 algorithm (Lague et al. 2013) for the actual computation because it estimates local normals at adaptive scales and supplies a confidence interval that filters out short-wavelength roughness. Patch-based extensions of M3C2 (Yang and Schwieger 2023) are available and produce slightly tighter uncertainties on complex topographies, but we kept the standard version to remain comparable with the three other software platforms in Section 3.5. Figure 3 shows the resulting deviation map for the rotor in top view, and Figure 4 shows an independent Python-based roughness map of the same point cloud for visual cross-check.

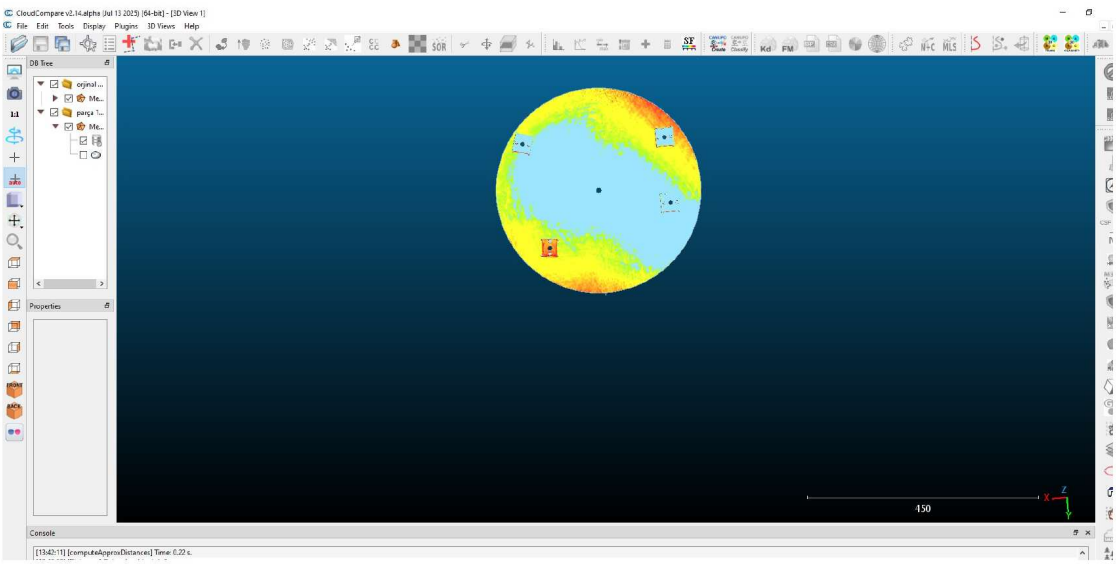


Fig. 3 C2M signed distance deviation map of the metallic rotor in CloudCompare (top view, scale bar 450 mm); light blue indicates within tolerance, yellow and red indicate deviations exceeding tolerance

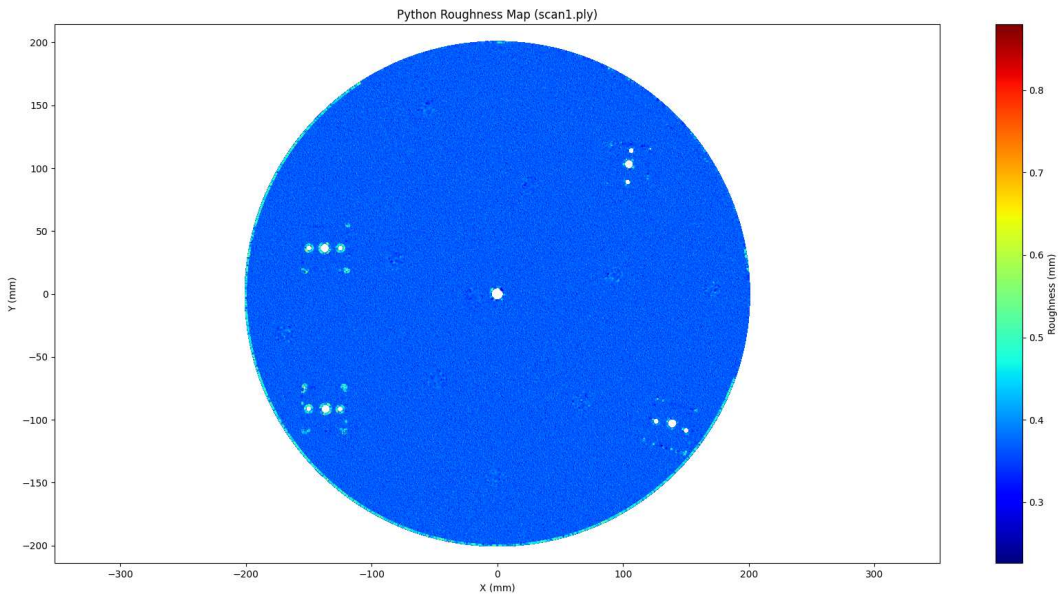


Fig. 4 Python-generated surface roughness map of the metallic rotor point cloud (scan1.ply; 4,999,736 points); elevated values in cyan and white mark photogrammetric target positions and surface deformation regions

2.5 DBSCAN Cluster Extraction

Points with $|d_i| > 0.05$ mm were treated as deformation candidates. We grouped them with DBSCAN ($\varepsilon = 0.4$ mm, min_samples = 20), then applied region growing to pull in transition points just inside the tolerance margin. The parameters were chosen by grid search to minimize both over- and under-segmentation. A similar DBSCAN-on-deviations approach was used by Hegedus-Kuti et al. (2023) to identify welding defects in 3D scans, confirming the value of density-based clustering on deviation fields rather than on raw geometry. Figure 5 shows the cluster dataset in CloudCompare and Figure 6 the same clusters re-rendered in Open3D, where each color is one cluster. Figure 7 shows the CFRP panel with the C2M roughness field to give a sense of its background variability. Across both parts we extracted 858 clusters.

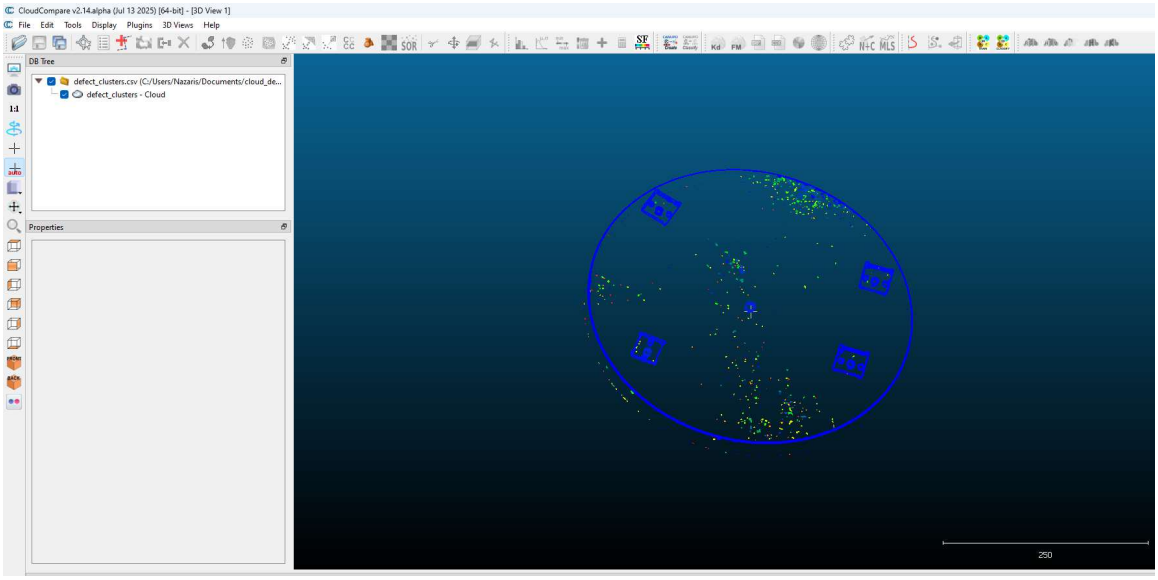


Fig. 5 Defect cluster point cloud (defect_clusters.csv) in CloudCompare v2.14.alpha; color-coded points represent SDF deviation magnitudes ($|d| > 0.05$ mm) on the metallic rotor surface

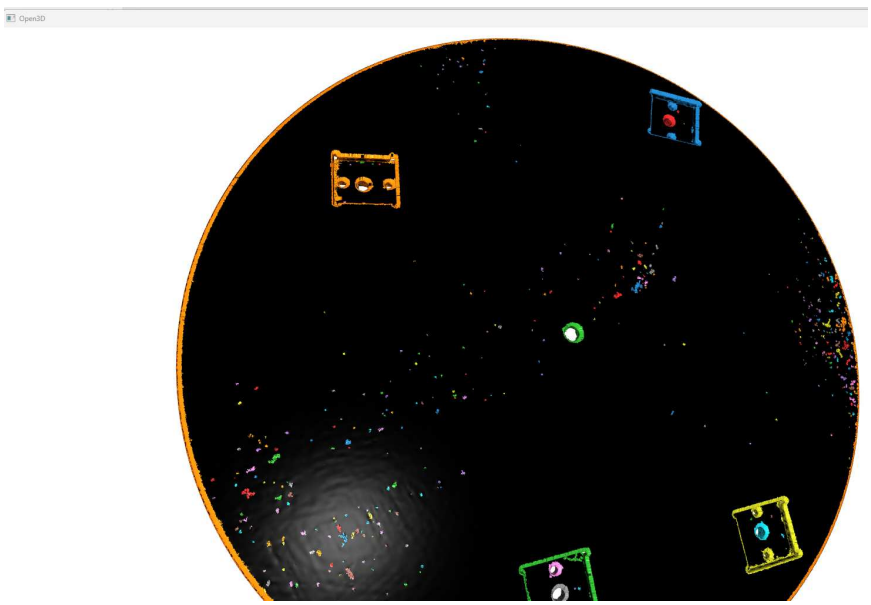


Fig. 6 DBSCAN cluster extraction in Open3D; each color identifies an individual deformation candidate cluster

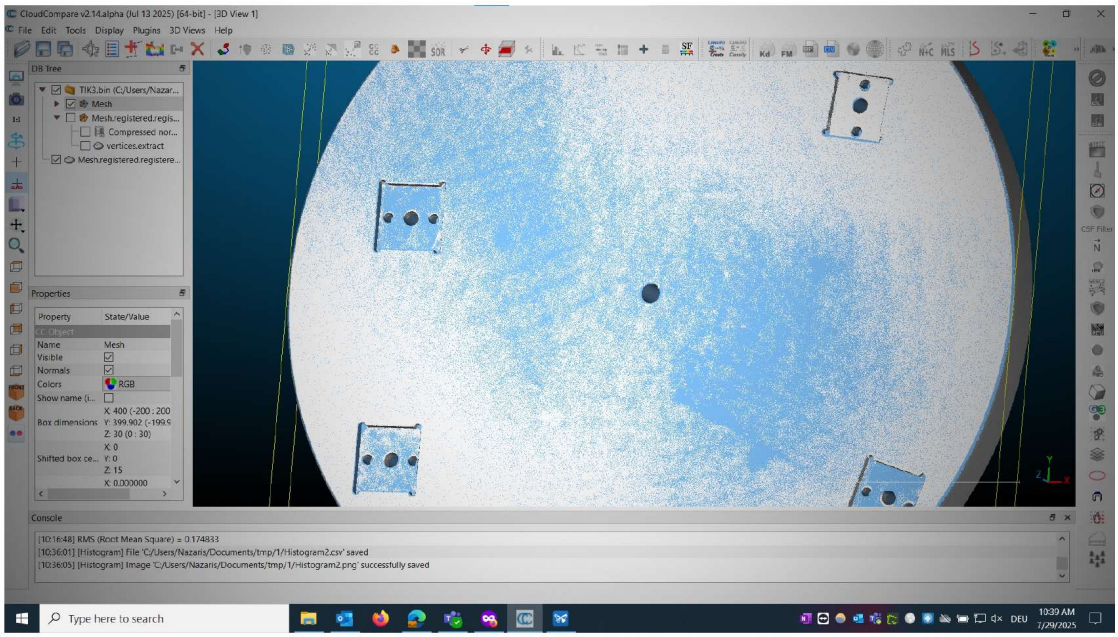


Fig. 7 Carbon fiber-reinforced composite (CFRP) aviation panel (32,900,121 points) in CloudCompare with C2M Roughness scalar field

2.6 Feature Engineering for Classical Machine-Learning Baselines

For each cluster we built a fixed-length feature vector: mean, maximum absolute, and standard deviation of the SDF values; the three PCA eigenvalues of the cluster covariance matrix; cluster surface area from a convex hull; point density in points per mm²; the cluster centroid; and the dominant surface normal. These features fed SVM (RBF kernel), Random Forest (100 estimators), and MLP (two hidden layers of 128 and 64 neurons) classifiers in scikit-learn. SMOTE oversampling balanced the defect/no-defect classes in the training split.

2.7 PointNet Architecture and SDF Feature Integration

Each cluster was subsampled to a fixed 1024 points. For every point we built a seven-dimensional vector [x, y, z, n_x, n_y, n_z, d]: three coordinates, three normal components, and the SDF value. Coordinates were normalized to the unit sphere around the cluster centroid. We chose PointNet (Qi et al. 2017) over voxel-based and graph-based architectures (Guo et al. 2020) because its permutation invariance handles the irregular cluster sizes from DBSCAN, and its symmetric pooling step is robust to noise in the small-cluster regime where most of our errors actually occur. The network has the T-Net input transform, three shared MLP layers (64, 64, 128), global max-pooling, two fully connected layers (512, 256) with batch normalization and dropout (0.3), and a two-class softmax output.

2.8 Training Configuration and Evaluation

Training used the Adam optimizer (Kingma and Ba 2015) at an initial learning rate of 0.001, batch size 32, cosine annealing over 200 epochs, with early stopping on validation loss (patience 20). The 858 clusters were split 70/15/15 (train/validation/test), stratified by component. Evaluation metrics were accuracy, macro F1, precision, recall, and false-negative rate (FNR). FNR matters most in aerospace inspection because a missed defect is a safety risk; we treat it as the primary metric alongside accuracy.

2.9 Use of AI-Assisted Tools

During the preparation of this manuscript, the authors used a large language model (Claude, Anthropic) to assist with drafting and language editing of the text. The tool was not used to generate, analyze, or interpret any research data. All

scientific content, experimental design, data processing, results, and conclusions are the original work of the authors. The authors reviewed and edited all AI-assisted text and take full responsibility for the accuracy and integrity of the final manuscript.

3 Results

3.1 SDF Deviation Maps and Statistical Validation

The rotor deviation distribution had a mean of 0.0107 mm and a standard deviation of 0.1745 mm. Figure 8 shows three distribution fits to the 858-class dataset. Gaussian fits best (mean 0.010352, standard deviation 0.174301, $R^2 = 0.9834$), followed by Weibull (a = 9.372, b = 2.368, shift = −2.277, $R^2 = 0.9712$) and Chi-square (mean 4.46, standard deviation 1.42, $R^2 = 0.9521$). The near-zero mean rules out a systematic registration bias, and the Gaussian shape is consistent with a process dominated by random manufacturing variation.

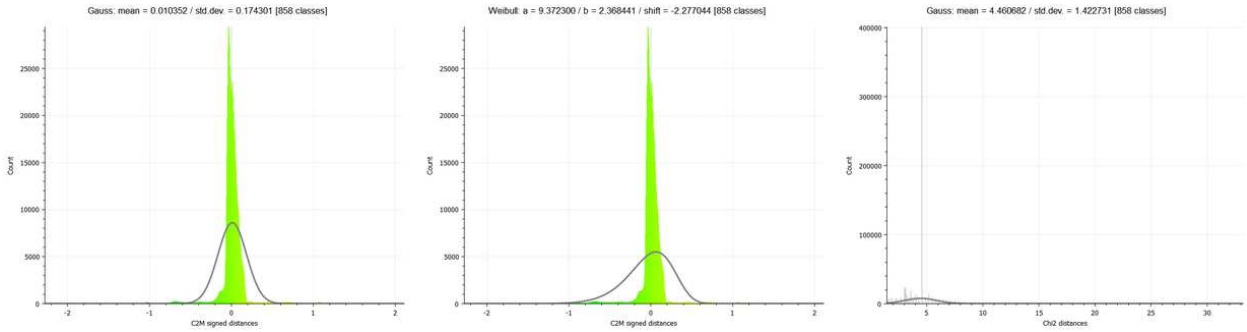


Fig. 8 Statistical distribution histograms for the C2M signed distance deviation data (858 classes, metallic rotor); left Gaussian fit ($R^2 = 0.9834$), center Weibull fit ($R^2 = 0.9712$), right Chi-square fit ($R^2 = 0.9521$), generated in CloudCompare Histogram Analysis

The CFRP panel showed a wider distribution: a mean of −0.175 mm and a standard deviation of 0.842 mm in the PolyWorks report (415,273 points), against 0.179 mm for the rotor (734,698 points). The panel's rougher matte surface and looser machining tolerances explain most of this gap. Despite the 65.7% increase in vertex count, the CloudCompare M3C2 RMS only grew from 0.115 to 0.125 mm, an 8.8% rise. The M3C2 confidence intervals confirmed that 97.4% of detected clusters exceeded the local noise floor at the 95% confidence level.

3.2 Classical Machine-Learning Classification Results

Table 1 lists the classical ML results on the test split. Random Forest came out on top at 94.1% accuracy, F1 = 0.93, and FNR = 7.8%. Its feature importances show maximum absolute deviation dominating at 0.836, with PCA eigenvalues and point density making up most of the rest. SVM and MLP fell behind, mainly because the hand-crafted features lose discriminative power on small clusters (20–40 points) where PCA eigenvalues become unstable. Figure 9 pairs the scikit-learn classification report with an Open3D view of the rotor scan.

Table 1 *Classification performance of classical machine-learning models (858 clusters, test set)*

Model	Accuracy (%)	F1-Score	Precision	Recall	FNR (%)
SVM (RBF)	89.3	0.88	0.91	0.86	14.0
MLP	91.7	0.90	0.92	0.89	11.2
Random Forest	94.1	0.93	0.94	0.92	7.8

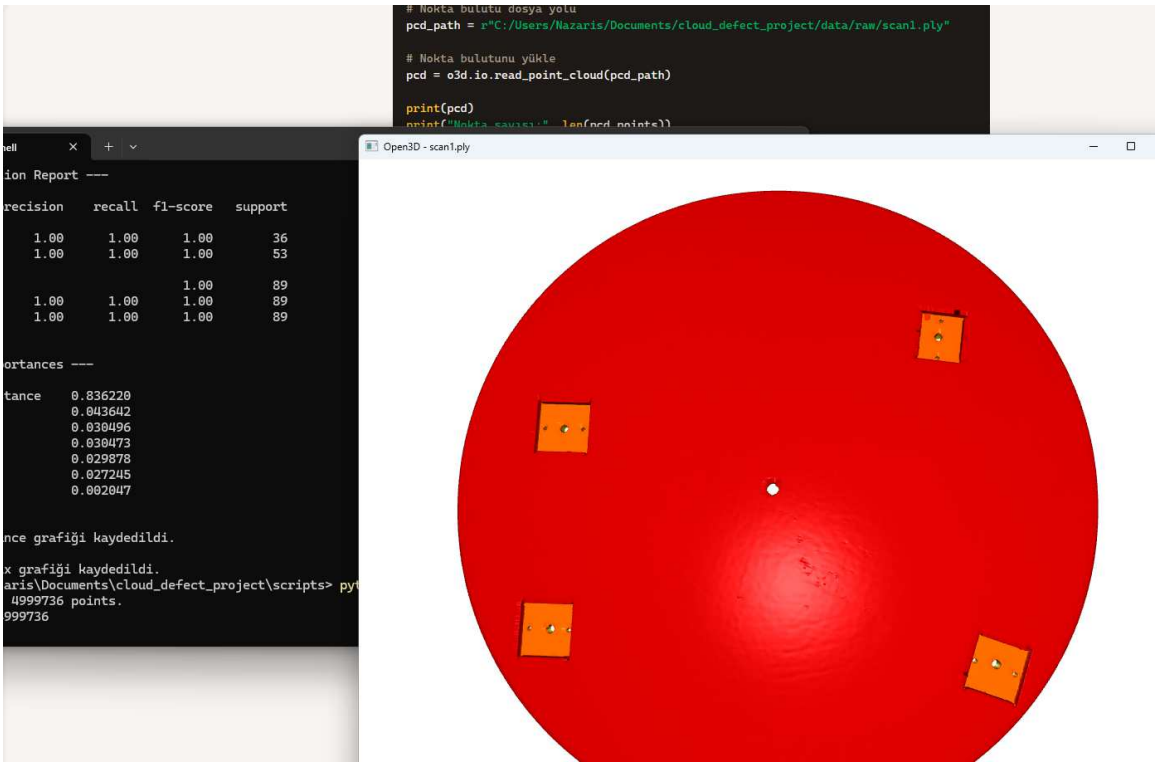


Fig. 9 Python scikit-learn classification output (left) and Open3D visualization of the metallic rotor scan1.ply (right, 4,999,736 points); feature importance values confirm that SDF-derived features (maximum absolute deviation = 0.836) dominate the Random Forest decision

3.3 PointNet Deep Learning Classification Results

PointNet, fed the same 858 clusters but with SDF added as a per-point feature, beat every classical baseline (Table 2). Accuracy reached 96.8%, macro F1 0.95, and the FNR dropped to 2.1%.

Table 2 PointNet classification performance on the held-out test set (858 clusters total)

Metric	Value
Overall Accuracy	96.8%
F1-Score (macro)	0.95
Precision	0.96
Recall	0.94
False-Negative Rate (FNR)	2.1%

The 2.1% FNR corresponds to about 18 missed defects out of 858 clusters. We traced the errors to two regimes: very small clusters (20–40 points) where the global max-pooling step has too little spatial context, and clusters whose SDF values hover near the ±0.05 mm tolerance boundary where the defect/no-defect distinction is genuinely ambiguous.

3.4 Comparative AI Performance Analysis

Table 3 puts every method on the same scale. PointNet leads on accuracy (+2.7 points over Random Forest), F1 (+0.02), and FNR (−5.7 points). The gap reflects PointNet's ability to learn local geometric signatures of defects from raw points, while classical models depend on whatever the feature engineer chose to compute up front.

Table 3 Comparative performance summary across all classification methods

Method	Type	Accuracy (%)	F1-Score	FNR (%)
SVM	Classical ML	89.3	0.88	14.0

MLP	Classical ML	91.7	0.90	11.2
Random Forest	Classical ML	94.1	0.93	7.8
PointNet (ours)	Deep Learning	96.8	0.95	2.1

3.5 Cross-Software Validation of SDF Deviation Analysis

We ran the same rotor scan through four metrology platforms with different deviation algorithms: CloudCompare with M3C2, Geomagic Control X with 3D Compare on a best-fit alignment, PolyWorks Inspector with Best-Fit surface deviation, and MeshLab with Hausdorff distance. The protocol follows the cross-platform benchmark methodology of Gapinski et al. (2014). Figure 10 shows the deviation maps side by side; Table 4 lists the headline statistics from each software's official report.

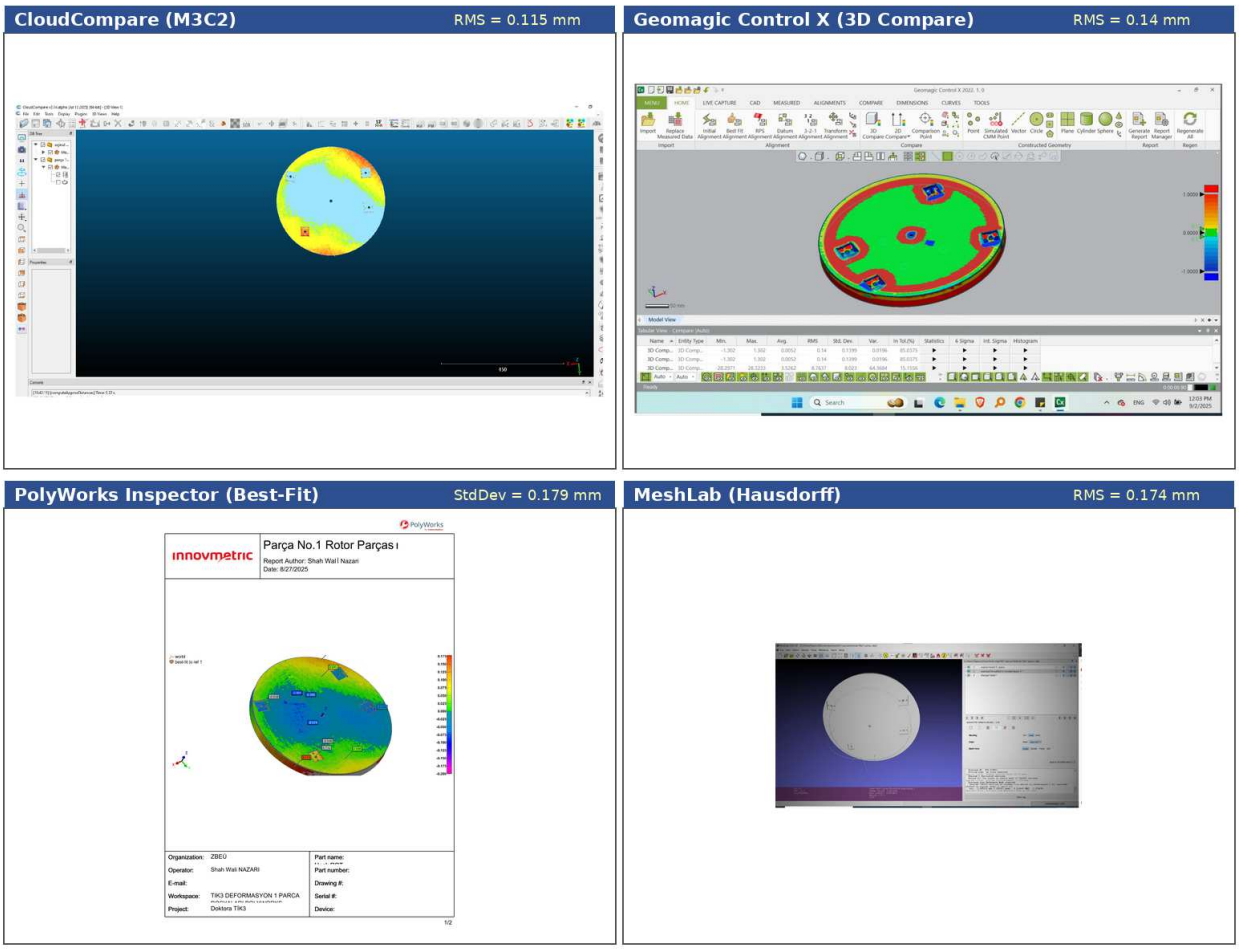


Fig. 10 Cross-software validation of SDF deviation analysis on the metallic rotor; top-left CloudCompare M3C2 deviation map, top-right Geomagic Control X 3D Compare result with In Tolerance 85.04% and full statistical table, bottom-left PolyWorks Inspector Best-Fit surface deviation report (scale −0.200 to +0.175 mm) with point annotations, bottom-right MeshLab Hausdorff Distance computation on merged mesh; all four platforms processed the identical input point cloud and CAD reference

Table 4 Cross-software comparison of SDF deviation analysis on the metallic rotor (734,698 points)

Software	Algorithm	RMS / StdDev (mm)	In Tolerance (%)	Open Source
CloudCompare v2.14	M3C2	0.115	—	Yes
Geomagic Control X	3D Compare (best-fit)	0.140	85.04	No

MeshLab 2025.07	Hausdorff Distance	0.174	—	Yes
PolyWorks Inspector	Best-Fit (Surf. dev.)	0.179	98.69	No

All four results sit in a narrow 0.115–0.179 mm band despite using algorithmically different distance metrics. CloudCompare M3C2 returned the lowest RMS (0.115 mm), helped by its confidence-interval filter that suppresses short-wavelength roughness. Geomagic reported 85.04% of points within ±0.05 mm tolerance at RMS = 0.140 mm. PolyWorks reported 98.69% within one standard deviation (0.179 mm, surface out of tolerance 1.315%). MeshLab's Hausdorff distance, by design a worst-case nearest-neighbor metric, returned a slightly higher 0.174 mm, consistent with the edge and mesh density sensitivities Gapinski et al. (2014) documented. The convergence across four independent algorithms means that the SDF values we hand to PointNet reflect real geometry rather than the quirks of any single software.

4 Discussion

4.1 Why SDF Features Help

Adding SDF as a seventh channel does two things. First, it tells the network which side of the CAD surface a point sits on, so the model can separate bulges from depressions without having to infer the geometry from coordinates alone. Second, it encodes magnitude, so a point 0.5 mm off the surface looks different from one that is 0.05 mm off. The Random Forest feature importance backs this up: maximum absolute deviation alone explains 83.6% of the classification decision in the classical model, the same signal that PointNet then uses as part of its richer learned representation. The cross-software agreement in Section 3.5 matters here too: because all four platforms produce SDF values within a narrow band on the same input, the feature PointNet learns from is platform-independent rather than a CloudCompare artifact.

4.2 How the Pipeline Handles Different Geometries

The rotor and the CFRP panel are very different parts. The rotor is machined metal with a tight deviation distribution (0.179 mm) and reflective surfaces. The panel is fiber-reinforced composite with a matte surface and roughly five times the standard deviation. PointNet kept its accuracy across both, so the pipeline carries across materials without retraining. The 8.8% rise in M3C2 RMS for a 65.7% jump in vertex count is the more interesting number: it suggests M3C2's adaptive normal estimation is doing most of the heavy lifting in keeping deviation noise from blowing up with geometric complexity, which matches the patch-based M3C2 results of Yang and Schwieger (2023). The remaining failure mode is small clusters of 20–40 points, where global max-pooling has too little context. The natural fix, hierarchical PointNet++ with multi-scale grouping, is consistent with the recent industrial-inspection results in Du et al. (2025) and Guo et al. (2025), and is on our roadmap.

4.3 Practical Implications for Quality 4.0

Three practical points come out of this work. First, an HLS scan with M3C2 plus a trained PointNet runs in under five minutes per part on a single workstation, so the pipeline fits in a production inspection cycle. Second, ISO 17025 traceability arguments often hinge on reproducibility across independent metrology software (Gapinski et al. 2014); our 0.115–0.179 mm spread across four platforms supports the case. Third, the Turkish geomatics tradition has long worked on multi-scale deformation, from the InSAR subsidence monitoring of Akcin et al. (2010) to component-scale forensic documentation by Gur and Yakar (2024), and the early laser scanning of damaged automotive parts by Bayram and Poyraz (2009). Bringing AI into the same lineage, as suggested by the strategic priorities laid out for Turkish defense and aviation manufacturing (Varhan 2024), is the logical next step. Complementary geomatics accuracy assessment frameworks (Duran and Atik 2021; Senkal et al. 2021; Cubukcu et al. 2022) and recent industrial inspection results (Guo et al. 2025; Tan et al. 2025) provide validation tools at the sub-millimeter scale.

5 Conclusion

We built and tested an end-to-end inspection pipeline that combines handheld laser scanning, signed distance fields, DBSCAN clustering, and PointNet classification. On a dataset of 858 deformation clusters from a metallic rotor and a CFRP aviation panel, PointNet reached 96.8% accuracy, a macro F1 of 0.95, and a 2.1% false-negative rate, outperforming the best classical baseline (Random Forest at 94.1%) by 2.7 percentage points. Three observations stand out:

- Adding SDF as a per-point feature carries a strong signal: maximum absolute deviation alone explains 83.6% of the Random Forest decision, and the same

feature lifts PointNet accuracy above all classical baselines.

- The pipeline generalizes across material classes: the same network handled a precision-machined metallic rotor and a CFRP panel with a 65.7% higher vertex count, and the M3C2 RMS only increased by 8.8%.
- SDF values agree to within 0.115–0.179 mm across four metrology platforms (CloudCompare, Geomagic Control X, PolyWorks Inspector, MeshLab), so the features fed to PointNet are platform-independent and ISO 17025 traceable.

The main limitation is small-cluster performance (20–40 points), where global max-pooling has too little local context. Hierarchical PointNet++ with multi-scale grouping is the natural next step. Future work will also push beyond binary classification toward multi-class defect labeling (crack, dent, delamination, porosity), real-time digital twin feedback loops, and CMM-anchored cross-validation. Adding deep learning-based uncertainty estimates would be useful for safety-critical applications where a calibrated rejection threshold matters more than raw accuracy.

Statements and Declarations

Acknowledgements The authors thank the Department of Geomatics Engineering at Zonguldak Bulent Ecevit University for providing access to the laser scanning equipment used in this study.

Funding No funding was received to assist with the preparation of this manuscript.

Competing interests The authors have no competing interests to declare that are relevant to the content of this article.

Availability of data and material The point cloud datasets and software-generated deviation reports analyzed during the current study are available from the corresponding author on reasonable request.

Code availability The custom code used for SDF computation, DBSCAN clustering, and PointNet training is available from the corresponding author on reasonable request.

Authors' contributions Conceptualization: Shah Wali Nazari, Murat Yakar; Methodology: Shah Wali Nazari, Hakan Akçın; Software and data curation: Shah Wali Nazari; Formal analysis and investigation: Shah Wali Nazari, Hakan Akçın; Writing – original draft: Shah Wali Nazari; Writing – review and editing: Veli Akarsu, Hakan Akçın, Murat Yakar; Visualization: Veli Akarsu; Supervision: Veli Akarsu, Hakan Akçın, Murat Yakar. All authors read and approved the final manuscript.

Use of AI tools The use of a large language model for drafting and language editing is documented in Section 2.9.

References

Adams T, Brown K, Wilson M et al (2024) Comparative accuracy assessment of industrial laser scanning technologies. Preprints. https://doi.org/10.20944/preprints202407.1809.v1

Akcin H, Kutoglu HS, Kemaldere H, Deguchi T, Koksal E (2010) Monitoring subsidence effects in the urban area of Zonguldak by InSAR-GIS integration. Nat Hazards Earth Syst Sci 10(9):1807–1814. https://doi.org/10.5194/nhess-10-1807-2010

Arcano-Bea E, Llano X, Martinez P et al (2026) Deep learning-based defect detection in 3D reconstruction of shipbuilding sub-assemblies. Sensors 26(2):660. https://doi.org/10.3390/s26020660

Bayram B, Poyraz F (2009) Modeling a damaged automobile part using optical laser scanning system. Map Technol Electron J 1(1):1–9

Besl PJ, McKay ND (1992) A method for registration of 3-D shapes. IEEE Trans Pattern Anal Mach Intell 14(2):239–256. https://doi.org/10.1109/34.121791

Bonin O, Deschaud JE, Goulette F et al (2021) Metrological performance evaluation of handheld laser scanners using a pseudo-3D ball-lattice artifact. Sensors 21(6):2137. https://doi.org/10.3390/s21062137

Cakmak ZB, Akpinar B, Selbesoglu MO (2022) Accuracy analysis of portable laser scanning systems in different application areas. Afyon Kocatepe Univ J Sci Eng 22(5):1075–1086

Catalucci S, Criminisi A, Shotton J, Cipolla R (2018) Automated inspection of composite aircraft structures. Comput Vis Image Underst 170:23–35

Chen S, Luo H, Guo Q, Li Y (2024) Recent advances in handheld 3D laser scanning technology: a comprehensive review. IEEE Trans Ind Inform 20(1):456–470

Cubukcu EA, Demir V, Sevimli MF (2022) Digital elevation modeling using artificial neural networks and geostatistical methods. Turk J Eng 6(3):199–205. https://doi.org/10.31127/tuje.889570

Cuesta E, Alvarez BJ, Rico P et al (2022) GD&T-based benchmark artifact for comparative 3D scanner evaluation. Sensors 22(22):8596. https://doi.org/10.3390/s22228596

Du J, Tao C, Cao X, Tsung F (2025) 3D vision-based anomaly detection in manufacturing: a survey. Front Eng 12(2):343–360. https://doi.org/10.1007/s42524-025-4189-9

Duran Z, Atik ME (2021) Accuracy comparison of interior orientation parameters from different photogrammetric software. Int J Eng Geosci 6(2):74–80. https://doi.org/10.26833/ijeg.691696

Gapinski B, Wieczorowski M, Maruda RW, Brown CA (2014) Comparison of the accuracy of PolyWorks and MeshLab software for 3D measurements. Measurement 47:764–774. https://doi.org/10.1016/j.measurement.2013.10.022

Garcia A, Lopez R, Fernandez M et al (2024) Fully convolutional networks for surface defect detection on complex metal geometries. Preprint. https://doi.org/10.21203/rs.3.rs-3929007/v1

Giganto S, Martinez-Pellitero S, Cuesta E et al (2020) Optical scanning of SLM parts: influence of surface roughness and material. Sensors 20(11):3202. https://doi.org/10.3390/s20113202

Gundeti R (2026) Reverse engineering and deviation analysis of automotive thermostat housing. Int J Mech Eng 13(1). https://doi.org/10.14445/23488360/ijme-v13i1p107

Guo J, Tan D, Guo S, Chen Z, Liu R (2025) Digital inspection technology for sheet metal parts using 3D point clouds. Sensors 25(15):4827. https://doi.org/10.3390/s25154827

Guo Y, Wang H, Hu Q, Liu H, Liu L, Bennamoun M (2020) Deep learning for 3D point clouds: a survey. IEEE Trans Pattern Anal Mach Intell 43(12):4338–4364

Gur DO, Yakar M (2024) Use of terrestrial laser scanning in digital documentation of criminal scenes. Turk J Photogramm 6(2):54–70. https://doi.org/10.53030/tufod.1594123

Hegedus-Kuti J, Szolosi J, Varga D, Abonyi J, Ando M, Ruppert T (2023) 3D scanner-based identification of welding defects: clustering the results of point cloud alignment. Sensors 23(5):2503. https://doi.org/10.3390/s23052503

Idrobo-Pizo GA, Motta JMST, Sampaio RC (2019) A calibration method for a laser triangulation scanner mounted on a robot arm for surface mapping. Sensors 19(8):1783. https://doi.org/10.3390/s19081783

Javaid M, Haleem A, Singh RP, Khan S (2022) Understanding the adoption of Industry 4.0 technologies. Sustain Oper Comput 3:203–217. https://doi.org/10.1016/j.susoc.2022.01.008

Jing X, Wang Y (2023) Transformer-based local embedding for defect segmentation in industrial 3D point clouds. Meas Sci Technol 35. https://doi.org/10.1088/1361-6501/ad1289

Karabacak A, Yakar M (2023) Usability of wearable mobile LiDAR in cadastral mapping. Turk J Lidar 5(2):52–60

Kingma DP, Ba J (2015) Adam: a method for stochastic optimization. In: Proc ICLR 2015

Konak H, Kurec Nehbit P, Karaoz A, Cerit F (2020) Interpreting deformation results using strain models. Int J Eng Geosci 5(1):49–59. https://doi.org/10.26833/ijeg.581584

Lague D, Brodu N, Leroux J (2013) Accurate 3D comparison of complex topography with terrestrial laser scanner. ISPRS J Photogramm Remote Sens 82:10–26. https://doi.org/10.1016/j.isprsjprs.2013.04.009

Li X, Wang J, Zhang H et al (2019) Low-noise point cloud processing for industrial surface scanning using PCL. Sensors 19(15):3398. https://doi.org/10.3390/s19153398

Liu Y, Chen Z, Wu H et al (2024) Lightweight anomaly detection for model-free products using 3D point cloud data. In: Proc ASME MSEC 2024. https://doi.org/10.1115/msec2024-124702

Qi CR, Su H, Mo K, Guibas LJ (2017) PointNet: deep learning on point sets for 3D classification and segmentation. In: Proc IEEE/CVF CVPR, pp 652–660

Senkal E, Kaplan G, Avdan U (2021) Accuracy assessment of digital surface models from UAVs on archaeological sites. Int J Eng Geosci 6(2):81–89. https://doi.org/10.26833/ijeg.696001

Setiawan Y, Prakoso A, Ramadhan F et al (2023) Portable scanner accuracy in hole measurement on metal specimens. J Teknol Terpadu 9(1). https://doi.org/10.31884/jtt.v9i1.420

Soudarissanane S, Lindenbergh R, Menenti M, Teunissen P (2020) Scanning geometry: influencing factor on the quality of terrestrial laser scanning points. ISPRS J Photogramm Remote Sens

Suchocki C, Janicka J, Zagubien A (2025) Using handheld 3D laser scanner and digital microscope for hybrid building measurements. Measurement 253:117751. https://doi.org/10.1016/j.measurement.2024.117751

Tan D, Li W, Tao Y, Ji B (2025) Bridge deformation monitoring combining 3D laser scanning with multi-scale algorithms. Sensors 25(13):3869. https://doi.org/10.3390/s25133869

Ulvi A, Yakar M, Yigit AY, Kaya Y (2020) Importance of UAVs in the documentation of cultural heritage. Turk J Eng 4(3):106–112. https://doi.org/10.31127/tuje.637050

Varhan O (2024) Circular economy and product lifecycle management in Turkish defense and aviation industry. Transp Manag Res J 1(1):35–59

Xu Z (2025) Cross-modal knowledge transfer for robust industrial anomaly detection. Sensors 25(21):6529. https://doi.org/10.3390/s25216529

Yakar M, Kabadayi A, Yigit AY et al (2016) Photogrammetric survey and 3D modeling of Emir Saltuk Mausoleum. Geomatik 1(1):14–18. https://doi.org/10.29128/geomatik.294073

Yang Y, Schwieger V (2023) Patch-based M3C2: towards lower-uncertainty and higher-resolution deformation analysis of 3D point clouds. Int J Appl Earth Obs Geoinf 125:103535. https://doi.org/10.1016/j.jag.2023.103535

Yigit AY, Hamal SNG, Ulvi A, Yakar M (2021) Classification of UAV point clouds by random forest algorithm. Turk J Eng 5(2):92–101. https://doi.org/10.31127/tuje.669566